Original Article
J. Korean Wood Sci. Technol. 2024, 52(5): 504-523
https://doi.org/10.5658/WOOD.2024.52.5.504

Journal of the Korean Wood Science and Technology
pISSN: 1017-0715 eISSN: 2233-7180
http://www.woodj.org

Synthesis and Characterization of Magnetic Cellulose Powder from Sawdust Waste

Heru SURYANTO[1,2,†] · Uun YANUHAR[3] · Husni Wahyu WIJAYA[4] · Joseph Selvi BINOJ[5] · Azlin Fazlina OSMAN[6] · Poppy PUSPITASARI[2] · Jibril MAULANA[7] · Nico Rahman CAESAR[3] · Fajar NUSANTARA[2] · Komarudin KOMARUDIN[2]

ABSTRACT

Timber industry waste is being examined for cellulose manufacturing to give important benefits. The study's goal is to investigate the properties of cellulose powder derived from sawdust waste after it has been reinforced with ferrous-ferric oxide nanoparticles (Fe_3O_4-NPs). Sawdust cellulose powder was produced from Sengon (*Albizia chinensis*) wood waste in this study. The crushed sawdust waste is handled with alkalization and bleaching. Cellulose powder is then reinforced with Fe_3O_4-NPs at 10 wt.%, 20 wt.%, and 30 wt.%. The magnetic cellulose powder was analysed by X-ray diffraction, Fourier Transform Infrared, scanning electron microscopy morphology, magnetic vibrating sample magnetometer, Brunauer-Emmett teller, and adsorption tests for Methylene Blue and Congo Red dyes. Structure study identifies sawdust as cellulose 1β, with peaks at 14°, 16°, and 22° diffraction angles. The addition of Fe_3O_4-NPs reduces the crystalline index of sawdust cellulose powder from 68.50% to 63.38%, and functional group bond analysis revealed many peak shifts indicating a change in the chemical bonds of magnetic cellulose powder. Incorporating Fe_3O_4-NPs into sawdust cellulose powder confers magnetic and superparamagnetic properties to the sawdust cellulose. Similarly, the surface texture of magnetic cellulose seems rougher as the surface area increases. These parameters imply a 31.8% increase in Congo Red adsorption, using adsorption kinetics based on the pseudo-first-order model.

Keywords: cellulose powder, dye adsorption, Fe_3O_4 nanoparticles, sawdust, waste

1. INTRODUCTION

Indonesia had a total population of 276.4 million in early 2023, with 58.2% living in urban centers while 41.8% living in rural areas (Kemp, 2023). In urban areas, the wastewater treatment capacity is limited to 0.3

Date Received May 16, 2024; Date Revised June 10, 2024; Date Accepted July 22, 2024; Published September 25, 2024
[1] Center of Science and Engineering (PSR), Universitas Negeri Malang, Malang, East Java 65145, Indonesia
[2] Center of Excellent for Cellulose Composite (CECCom), Department of Mechanical and Industrial Engineering, Universitas Negeri Malang, Malang, East Java 65145, Indonesia
[3] Department of Aquatic Resources Management, FPIK, University of Brawijaya, Malang, East Java 65145, Indonesia
[4] Department of Chemistry, FMIPA, Universitas Negeri Malang, Malang, East Java 65145, Indonesia
[5] Institute of Mechanical Engineering, Saveetha Institute of Medical and Technical Sciences (SIMATS), Saveetha University, Chennai 602105, India
[6] Faculty of Chemical Engineering Technology, Universiti Malaysia Perlis, Perlis 02600, Malaysia
[7] Faculty of Vocational, Universitas Negeri Malang, Malang, East Java 65145, Indonesia
[†] Corresponding author: Heru SURYANTO (e-mail: heru.suryanto.ft@um.ac.id, https://orcid.org/0000-0001-7037-1868)

km^3/year despite the estimated 14.30 km^3/year total volume of wastewater (Widyarani *et al.*, 2022). Wastewater degrades water quality and endangers human health and aquatic biota (Sharma, 2015), so wastewater management has been a major challenge in the last decade (Renu *et al.*, 2017).

Environmental pollution has consistently posed a significant issue, not only hindering industrial progress but also endangering public health. Organic dyes constitute a major pollution source given their extensive use in textile, paper, cosmetics, and various other sectors (Hanafi and Sapawe, 2020; Rani and Shanker, 2023). However, most of these dyes are harmful, possessing toxicity, carcinogenicity, and teratogenicity (Ivanova *et al.*, 2023), and are challenging to naturally degrade through photodegradation or biodegradation (Groeneveld *et al.*, 2023). Conventional wastewater treatment methods to reduce pollutants include oxidation and physical-chemical using activated carbon (Jiang *et al.*, 2019), flocculation/coagulation (Barros *et al.*, 2022), adsorption (Rashid *et al.*, 2021), and membrane technology (Giacobbo and Bernardes, 2022). The use of synthetic and natural polymers is more widely used than inorganic adsorbents. Inorganic adsorbents have the disadvantage of being non-biodegradable, expensive, and nonselective (Sukmana *et al.*, 2021). Efforts to reduce and improve the performance of natural adsorbent are needed so that the results of the adsorption process become biodegradable and ready to be disposed of to reduce overall costs by using cellulose from sawdust waste as an adsorbent.

Cellulose stands as the most abundant biopolymer on the earth with annual production of about 1.5×10^{12} tons (Mahsuli *et al.*, 2023). Total trade reached $5.86 billion in 2019 (Suryanto *et al.*, 2023), and it is projected that by 2026, the cellulose trade will attain a value of approximately USD 305.08 billion (Fortune Business Insight, 2024) and most cellulose is derived from wood pulp. Indonesia's 2017 log production reached 43.0 million m^3 (Hadi *et al.*, 2020) and increase in 2019 reached 48.0 million m^3 (Haryanto *et al.*, 2021) and with an estimated sawdust of 2 million m^3/tahun (Mwango and Kambole, 2019), sawdust is a promising source for cellulose production. Several researchers reported sawdust can be extacted as natural dye (Mindaryani *et al.*, 2023; Rahman *et al.*, 2021), wood ceramics (Hwang and Oh, 2023, 2024), wood pellet (Yang *et al.*, 2019), activated charcoal (Sutapa *et al.*, 2024), board composite (Hwang and Oh, 2020, 2021) and as a low-cost absorbent (Kheradmand *et al.*, 2022; Rahman *et al.*, 2022). However, separating sawdust from treated wastewater is difficult and takes a long time (Teixeira *et al.*, 2021). Besides, the cellulose surface has a low charge density that influences the dye adsorptive mechanism (Hussain *et al.*, 2018). However, natural polymers like cellulose tend to degrade over time, causing lower floc stability and strength during the coagulation-flocculation process (Lee *et al.*, 2012) and lower efficiency (Stefan *et al.*, 2022). Increasing the performance of cellulose in dye adsorption has been carried out by making it a chemical modification through surface functionalization or copolymerization of cellulose ether (Koshani *et al.*, 2020; Li *et al.*, 2021) or by adding particles such as MoS_2 (Thangavelu and Zou, 2022).

In recent years, there has been an increasing fascination with the progress of cellulose nanocomposites. Biodegradable polymers sourced from natural materials have sparked considerable interest due to environmental challenges like global warming and stringent regulations on polymer disposal (Gwon *et al.*, 2018). These composites, reinforced with nanomaterials, can alter the characteristics of the nanocomposite material, resulting in additional and unique functionalities. Hydrophilic properties are attributed to Fe_3O_4 nanoparticles (Fe_3O_4-NPs), which facilitate the development of molecular bonds between hydroxyl groups and oxygen due to the surplus electrons

from the hydroxyl groups (Kameya and Yabe, 2019) type of molecular bond is generated by the attractive force of the fibril to Fe_3O_4-NPs. Furthermore, the inclusion of mechanical interlocking further restricts the movement of cellulose fibrils by Fe_3O_4-NPs, consequently enhancing the mechanical properties of the nanocomposite (Elsacker *et al.*, 2021; Yu *et al.*, 2021). Remarkably, Fe_3O_4 systems have demonstrated efficacy in disinfecting coliform and enterococcus bacterial communities (Padmanabhan *et al.*, 2021) and increasing the charge capacitance ability of cellulose material (Yamklang *et al.*, 2023). Efforts to facilitate the separation system in wastewater treatment are made by functionalizing Fe_3O_4 magnetic nanoparticles into cellulose so they will be easily separated with a magnet when applied as a wastewater coagulant or dye adsorbent. So, the objective of this study is to observe the characteristics of sawdust cellulose powder (SCP) of Sengon (*Albizia chinensis*) wood with the functionalization of magnetic nanoparticles of Fe_3O_4 for dye removal from wastewater. The properties of the adsorbent were identified by testing procedures, including crystallinity of magnetic cellulose structure using X-ray diffraction (XRD), functional group analysis using Fourier transform infrared (FTIR), morphology using scanning electron microscope (SEM), magnetic properties analysis using vibrating sample magnetometer (VSM) and porosity using Brunauer Emmett Teller (BET), and dye adsorption using UV-Vis spectrometer.

2. MATERIALS and METHODS

2.1. Materials

The magnetic cellulose used sawdust waste of Sengon wood with an age of about 5 years, obtained from Malang Regency, Indonesia. Chemical reagents in this study include sodium hydroxide/NaOH (Merck, Singapore), hydrogen peroxide/H_2O_2 (Merck), Fe_3O_4-NPs with particles size of 30−50 nm (Guangzhou Hongwu Material Technology, Guangzhou, China), and Methylene Blue and Congo Red dye (Surya Techno Chemlab, Jawa Timur, Indonesia).

2.2. Alkalization process

The sawdust was crushed to make it powdery for 10 minutes. Sawdust powder passed with 80 mesh sieve was used for further process. 100 grams of powder was immersed in 4 liters of water for 1 week, with the water changed every 2 days to clean material that was dissolved by water. The sawdust powder is then oven-dried at 110℃−120℃ for 20 hours. Each 4 grams of powder was then alkalized with 80 mL of 5% NaOH (w/v) solution carried out on hot plate at 180℃ for 3 hours. Sawdust powder was rinsed 4 times and soaked for 3 hours with 500 mL distilled water. The alkalization process was repeated 4 times.

2.3. Bleaching cellulose

10% dry SCP was mixed with 10% H_2O_2 solution (5 g cellulose for 100 mL H_2O_2), then the pH was adjusted to 11.5 with sodium hydroxide and stirred for 30 minutes at 80℃. Once the reaction occurred, the SCP was separated from the solution using vacuum filtration. SCP was washed several times to get pH 7.0 and then dried using air drying for 1−3 days.

2.4. Cellulose/Fe_3O_4 nanoparticles synthesis

Distilled water (100 mL) in a beaker glass was added by Fe_3O_4-NPs with each concentration of 0.0wt% or control (SCPFe0), 10.0wt% (SCPFe10), 20.0wt% (SCPFe20), and 30wt% (CFe30), then sonicated at 20 kHz, 30 minutes. Each Fe_3O_4-NPs content was added by

5 g of dried SCP to form an SCP composite. The mixture was stirred for 30 minutes, and sonication was carried out to reduce agglomeration at 20kHz for 30 minutes. SCP composite was oven-dried at 60℃ for 20 hours.

2.5. Crystallinity analysis

The crystallinity of the SCP composite was observed by XRD (X'pert Pro, Malvern Panalytical, Westborough, MA, USA). Powder samples were scanned using XRD at 2θ of 5°−90°, 30 mA and 40 kV, and a wavelength of 1.542 Å. Scherrer's formula [Equation (1)] and Segal formula [Equation (2)] were used to calculate crystallite size (L) and crystalline index (CI), respectively (Yanuhar *et al.*, 2022).

$$L = \frac{Kl}{b\cos q} \quad (1)$$

Where q was the angle of diffraction; b was FWHM (rad); l was the X-ray wavelength; K was 0.89 (Scherrer's constant).

$$CI = \frac{I_{[002]} - I_{[am]}}{I_{[002]}} \times 100\% \quad (2)$$

Where: $I_{[002]}$ is the maximum intensity of [002] lattice diffraction at about 22.0° and $I_{[am]}$ is the lowest intensity at about 18°.

2.6. Characterization of sawdust cellulose powder composite

Characterization of SCP composite included the analysis of functional group, morphology, and magnetic properties. The SCP composite functional groups were analyzed using FTIR (Prestige-21, Shimadzu, Kyoto, Japan). SCP composite was dried at 105℃ for 3 h in the oven and then ground into powder. KBr powder 1.0 mg was mixed with SCP powder 0.1 mg and then pressed to form a pellet. The sample was scanned in the wavenumber ranging from 400 to 4,000 cm^{-1} at a rate of 2.0 cm^{-1}. SCP composite powder morphology was observed under an SEM (Inspect S50, FEI, Tokyo, Japan) at 25 kV. A gold coating (SC7 620, Emitech, Chelmsford, UK) was applied to the SCP composite powder before being observed under SEM. VSM (PPMS-VersaLab, Quantum Design, San Diego, CA, USA) analysis was conducted on SCP powder samples with a minimum mass of 50 mg to observe magnetic properties. VSM applied a magnetic field from −3,000 Oe to 3,000 Oe at room temperature (25℃) to the sample. BET analysis (Micromeristic Instrument, Norcross, GA, USA) with nitrogen gas as an adsorbate medium was applied to the sample to obtain the specific surface area and porosity of the SCP composite. Before analysis, the sample was degassed at 105℃ for 4 h. BET test was conducted at standard temperature and pressure (STP; 273.15 K and atmospheric pressure; 1.013×10^5 Pa).

2.7. Dye adsorption

Three sample measurements of dye adsorption were conducted using a UV-VIS spectrophotometer (Thermo Fischer Scientific, Waltham, MA, USA). The standard solution was prepared by adding 100 mg of Methylene Blue into 1,000 mL of distilled water, resulting in 100 ppm of the main solution. Then, dilute this main solution to reduce the concentration to 4 ppm in 100 mL. Add the SCP composite (0.5 g) into the solution and stir for 30 min. The analysis's maximum wavelength was 662 nm, and the absorbance was used to calculate the amount of Methylene Blue left in the effluent after the adsorption process. The following equation [Equation (3)] can be used to calculate the percentage of dye removed (Rd) from polluted water:

$$Rd = \frac{Co - C}{Co} \times 100\% \quad (3)$$

Where Co and C are the dye concentrations before and after treatment (mg/L), respectively.

The results of dye removal were analyzed using one-way ANOVA with a significant level of 95%.

The kinetic adsorption of dye was modeled using two different kinetic models: pseudo-first-order and pseudo-second-order models expressed by Equations (4) and (5), respectively (Al-Harby *et al.*, 2021).

$$Log(q_e - q_t) = Log\ q_e - \frac{K1}{2.303}t \quad (4)$$

$$\frac{t}{q_t} = \frac{1}{K_2 q_e^2} + \frac{t}{q_e} \quad (5)$$

Where q_e and q_t are the adsorption capacity at equilibrium time and time t (mg/g), respectively, K1 is the pseudo-first-order rate constant (1/min), and K2 is the pseudo-second-order constant [g/(mg. min)]; t is the time (min). For pseudo-first-order, the values of qe and K1 were determined from the intercept and the slope of the linear plot of Log (q_e − q_t) versus t. For the pseudo-second-order, q_e and K_2 were determined from the slope and intercept of the linear plot of t/q against t.

3. RESULTS and DISCUSSION

3.1. Morphology analysis

SCP is constructed of multiple cellulose chains, which are stabilized by van der Waals forces and hydrogen bonds (Zhang *et al.*, 2019). Incorporating Fe_3O_4-NPs into SCP leads to the change in SCP color from yellowish to blackish powder formation of a powdered morphology, as illustrated in Figs. 1 and 2.

SCPFe0 shows a fiber structure with fiber walls and the lumen [Fig. 2(a)] with a smooth surface. After *ex-situ* nanoparticles, the SCP surfaces are successfully loaded on the Fe_3O_4-NPs [Fig. 1(b–d)]. SCPFe10 indicates several Fe_3O_4-NPs are deposited on the surface [Fig. 2(b)]. Fe_3O_4-NPs lead to agglomeration in SCPFe20, causing a rougher morphology [Fig. 2(c)]. The roughness of the SCP nanocomposite is derived from Fe_3O_4-NPs, and the rougher surface increases with the increasing Fe_3O_4-NPs content. This effect arises from the natural tendency of Fe_3O_4-NPs to adhere to nearby particles and form aggregates. Increasing Fe_3O_4-NPs content of 30.0wt% leads to more agglomeration on the surface SCPFe30 [Fig. 2(d)]. In addition to being applied onto the surface, the Fe_3O_4-NPs are combined with SCP, resulting in further clumping of the Fe_3O_4-NPs within the SCP. This phenomenon is a characteristic trait

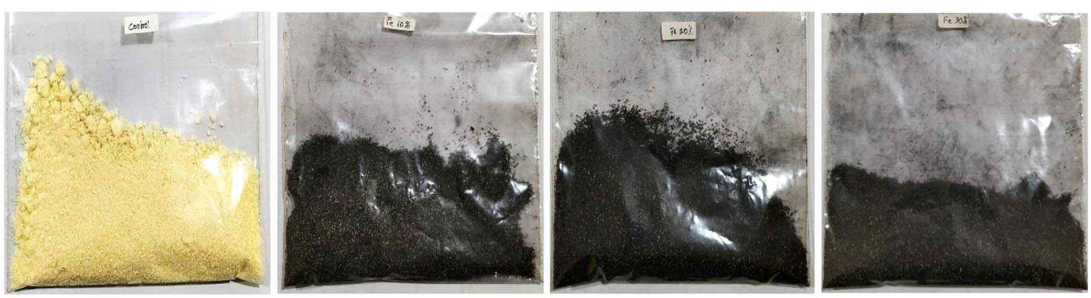

Fig. 1. SCP composite powder sample of (a) control (SCPFe0), (b) SCPFe10, (c) SCPFe20, and (d) SCPFe30. SCP: sawdust cellulose powder.

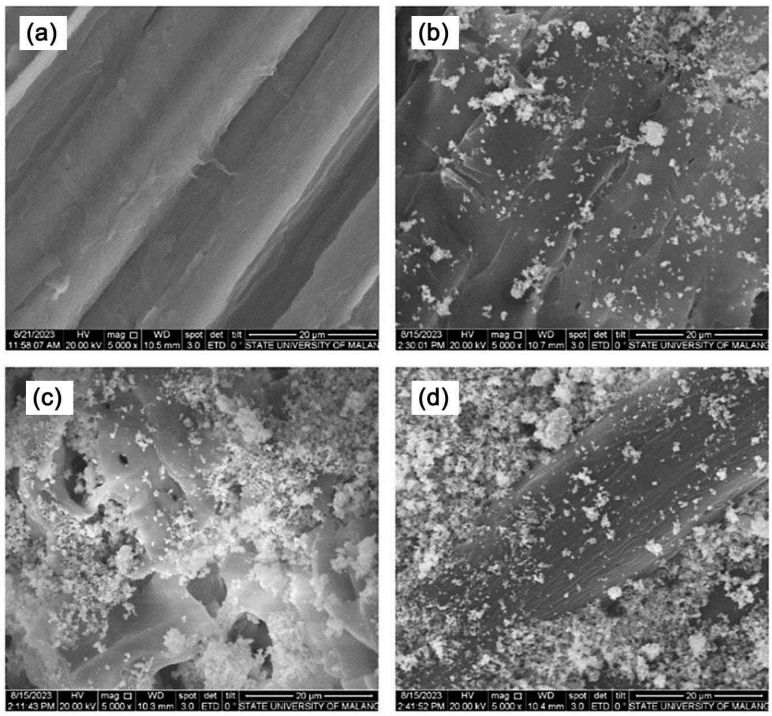

Fig. 2. Morphology of SCP with (a) control (SCPFe0), (b) SCPFe10, (c) SCPFe20, and (d) SCPFe30 (bar = 20 μm). SCP: sawdust cellulose powder.

of nanoparticles that tend to agglomerate and form large-sized aggregates in aqueous medium strongly (Kędzierska *et al.*, 2021). The magnetic properties of Fe_3O_4-NPs make them easier to agglomerate because of their high surface energy (Rahmawati *et al.*, 2018). Furthermore, the Fe_3O_4-NPs display a favorable affinity with cellulose due to hydrogen bonding interactions (Zhang *et al.*, 2019). However, a substantial interaction between the Fe_3O_4-NPs and cellulose can influence the overall morphology of the SCP.

3.2. Analysis of sawdust powder crystallinity

Fig. 3 illustrates the diffraction peaks of the SCP nanocomposite. The SCP nanocomposite indicates a structure of cellulose Iβ with peaks at 15.1, 16.5, 22.8, and 34.4 corresponding to the lattice plane of [110], [1$\bar{1}$0], [200], and [004], respectively (Lee *et al.*, 2015; Nindiyasari *et al.*, 2016). The presence of Fe_3O_4-NPs is indicated in SCP at 2θ of 30.5°, 35.6°, 43.2°, 53.6°, 57.1°, 62.7°, 71.1°, 74.1°, and 86.8°, correspond to the lattice plane of [220], [311], [400], [422], [511], [440], [620], and [622], respectively (JCPDS No. 19-0629). The diffraction peaks spanning the 2θ range of 10°–90° displayed marginal alterations, although the intensity of distinct diffraction peaks amplified as the Fe_3O_4-NPs content increased. The notable presence of Fe_3O_4-NPs in the SCP was discernible, presumably due to their accumulation on the SCP surface. Nonetheless, higher concentrations of Fe_3O_4-NPs increase the aggregation of nanoparticles, leading to a more evident crystalline quality. Those peaks were also observed with relatively low intensities in SCPFe10 and SCPFe20 samples. This indi-

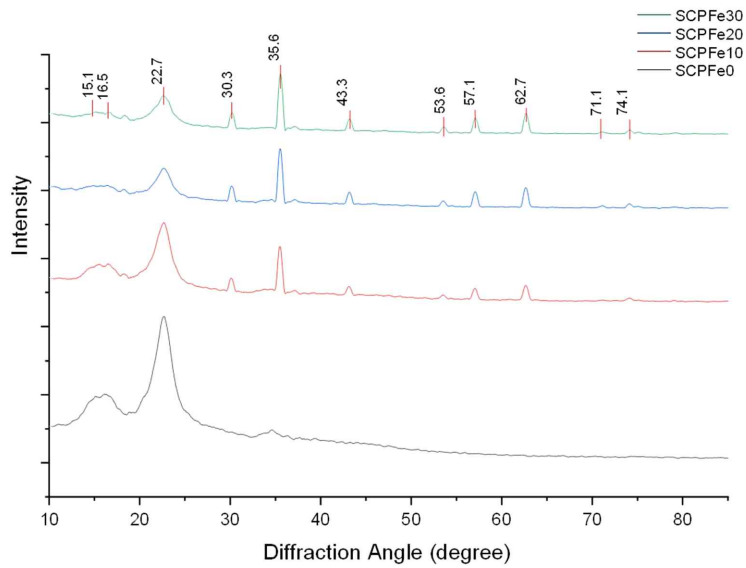

Fig. 3. Diffraction pattern of SCP with Fe_3O_4-NPs reinforcement. SCP: sawdust cellulose powder, Fe_3O_4-NPs: Fe_3O_4 nanoparticles.

cated that the number of Fe_3O_4-NPs formed was greatest in the SCPFe30 sample. The cellulose arrangement becomes random due to the greater Fe_3O_4-NPs content, and the crystal value also decreases (Kiangkitiwan and Srikulkit, 2021).

The CI value of SCPFe0 is 68.6% (Table 1). Fe_3O_4-NPs content of 10.0 wt%, 20.0 wt%, and 30.0 wt% reduces the CI value of 67.91%, 66.15%, and 63.58%, respectively. The crystallite size of the SCP composite is 12.18, 13.08, 15.35, and 15.75 nm for the SCPFe0, SCPFe10, SCPFe20, and SCPFe30, respectively. The introduction of Fe_3O_4-NPs resulted in a noticeable augmentation of the crystallite size, possibly due to the incorporation of Fe_3O_4-NPs into the SCP framework, which inherently possesses larger crystallites ranging from 9 to 53 nm (Upadhyay *et al.*, 2016). The crystallinity of wood's cellulose is influenced by rearrangement of the cellulose molecules in quasicrystalline region (Bhuiyan *et al.*, 2000). In this case, higher content of Fe_3O_4-NPs might facilitate the damage of arrangement of cellulose molecule leading to a lower crystallinity index or the crystalline structure of SCP was damaged by magnetization (Dong *et al.*, 2016). Contrastly, higher Fe_3O_4-NPs content influence to broadening of crystalline cellulose peaks and decreased in amplitude (Wotton *et al.*, 2021) so crystallite size decreased.

Table 1. Crystallinity of SCP composite

Sample	Intensity (a.u.)		Crystallinity parameter	
	$I_{22.5}$	I_{18}	CI (%)	L (nm)
SCPFe0	433.29	136.48	68.50	12.18
SCPFe10	244.09	78.336	67.91	13.08
SCPFe20	135.15	45.751	66.15	15.35
SCPFe30	121.74	44.333	63.58	15.75

SCP: sawdust cellulose powder, CI: crystalline index.

3.3. Functional group analysis

The SCP composite underwent FTIR analysis, and

the results of these tests are depicted in Fig. 4. IR transmittance spectrum was captured for SCPFe0, indicated by the black curve, as well as for varying content of Fe_3O_4-NPs functionalized SCP (10.0 wt%, 20.0 wt%, and 30.0 wt%). The analysis encompassed a wavenumber from 400 to 4,000 cm^{-1}.

Comparing the IR spectrum of the SCP-Fe_3O_4-NPs reinforcement with the SCP, some peak changes were detected. Fig. 3 is a representation of the intermolecular bonding of the SCP-Fe_3O_4-NPs composite. According to Fig. 4, introducing Fe_3O_4-NPs into SCP leads to a displacement of the C-H and O-H stretching signals within wavenumber of 2,700–3,600 cm^{-1}, originating from cellulose (Suryanto *et al.*, 2019). The wide peak observed within the 3,300–3,600 cm^{-1} range corresponds to the vibrational stretching of OH groups, which plays a pivotal role in defining hydrogen bonding (Wiguna *et al.*, 2023). Some changes occur at several points of the wavelength value. The O-H bond at 3,600 cm^{-1} disappears after adding Fe_3O_4-NPs. This suggests that the presence of Fe_3O_4-NPs alters the hydrophilicity properties of SCP. Besides that, at the point of 2,900 cm^{-1}, which is a representation of the C-H bond, it also experiences valley loss. In wavenumber from 760 to 1,800 cm^{-1}, the spectrum exhibits modes of organic groups (Lesiak *et al.*, 2019). The cellulose peak within the wavenumber from 1,520 to 400 cm^{-1} exhibits broadening due to the flexing of functional groups like CH_2, C-H, and C-O within the cellulose structure (Suciyati *et al.*, 2021). At wave number 1,589 cm^{-1}, the C = O double bond experienced a decrease in the transmittance value, indicating a reduced number of these bonds (Mitić *et al.*, 2009). The wave numbers 1,156 cm^{-1} and 894 cm^{-1} also experience loss of transmittance peaks, which references the C-O-C bond. The emergence of new transmittance peaks at points 563 cm^{-1} and 430 cm^{-1} indicates the presence of Fe-O bonds (Kamakshi *et al.*, 2019).

3.4. Magnetism analysis

Different factors, including attributes like crystallinity,

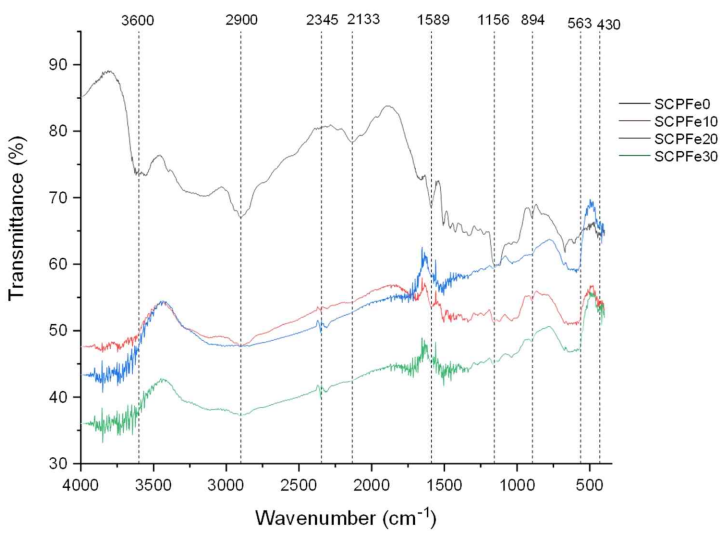

Fig. 4. Infrared spectrum for SCP composite with Fe_3O_4-NPs reinforcement. SCP: sawdust cellulose powder, Fe_3O_4-NPs: Fe_3O_4 nanoparticles.

dimensions, morphology, and imperfections in the crystal lattice, play a substantial role in influencing magnetic attributes. Magnetic properties of SCP nanocomposite were identified using the hysteresis loops analysis between Magnetization (M) and applied field (H) using the VSM apparatus at room temperature. The hysteresis loops illustrating the SCP composite are presented in Fig. 5. The amount of such saturation magnetization (Ms), remanent magnetization (Mr), and magnetic coercivity (Mc) become the basis for the analysis of the magnetic properties of SCP nanocomposite, as shown in Fig. 5 and Table 2. The SCPFe0, as the control sample, has no hysteresis curve that indicates a diamagnetic material. After adding Fe_3O_4-NPs, the SCP composite indicates the magnetic properties shown by the small hysteresis curve. The small hysteresis curve suggests that magnetic cellulose possesses a superparamagnetic characteristic (Daoush, 2017). When subjected to an external magnetic field, the magnetic cellulose exhibiting superparamagnetic attributes can become magnetized and drawn toward the magnetic field. Nevertheless, the magnetization of the cellulose materials cannot be sustained once the external magnetic field is withdrawn (Sezer *et al.*, 2021).

Fig. 5(a) depict whole VSM graph of SCPFe composite and Fig. 5(b) is deconvulation of VSM graph that shows the small Mc of the SCP composite, which is nearly negligible, and the low Mr value (Table 2), indicating that the SCP composite shows paramagnetic characteristics. This property renders the material valuable for applications in nanotechnology and biomedical fields, including drug delivery systems (Palanisamy and Wang, 2019), magnetic separation techniques (Nithya *et al.*, 2021), and scenarios in biomedicine that require controlled and reversible magnetic responses (Xiao and Du, 2020). The higher Fe_3O_4-NPs content, the higher Ms. SCPFe0, SCPFe10, SCPFe20, and SCPFe30 have Ms of 0.0, 0.01, 0.02, and 0.04 emu/g at 3,000 Oe (Table 2).

Compared to the other samples, SCPFe30 shows the largest energy dissipation rate, as seen from the hysteresis loop. This indicates that the SCPFe30 sample has the capacity to retain most of the saturated magnetic field even after the driving field is withdrawn (Usawattanakul *et al.*, 2021). The increase in Ms is attributed to the existence of the Fe_3O_4 on the particle surface due to an

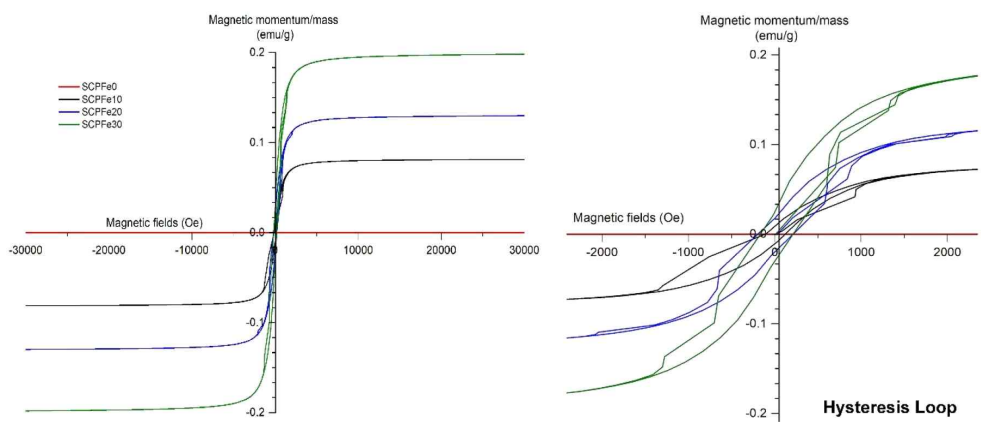

(a) (b)

Fig. 5. VSM graphs of SCPFe composite (a); Deconvulation of hysteresis loop (b). SCP: sawdust cellulose powder, VSM: vibrating sample magnetometer.

Table 2. Magnetic characteristics of SCPFe composite

Sample	Ms (emu/g)	Mr (emu/g)	Mc (Oe)
SCPFe0	0.00	0	0
SCPFe10	0.01	0.063	99.40
SCPFe20	0.02	0.114	87.50
SCPFe30	0.04	0.175	239.16

SCP: sawdust cellulose powder, Ms: saturation magnetization, Mr: remanent magnetization, Mc: magnetic coercivity.

effective modification reaction on the nanoparticles (Laksono *et al.*, 2023; Movagharnezhad *et al.*, 2022). The study conclusively indicates that increasing the content of magnetic material will enhance the magnetic properties of the composites for the intended application. Greater Ms values lead to increased magnetic induction within their surrounding area. This quality proves advantageous in magnetic separation processes, as it guarantees that the magnetic particles or isolated constituents are thoroughly magnetized and easily drawn toward the magnetic field. This enhancement in magnetic response subsequently improves the efficiency of the separation process.

3.5. Brunauer Emmett Teller analysis

The BET analysis result of SCP composite using the adsorption of nitrogen is shown in Fig. 6, with no hysteresis loop in the sample, which indicates a homo-

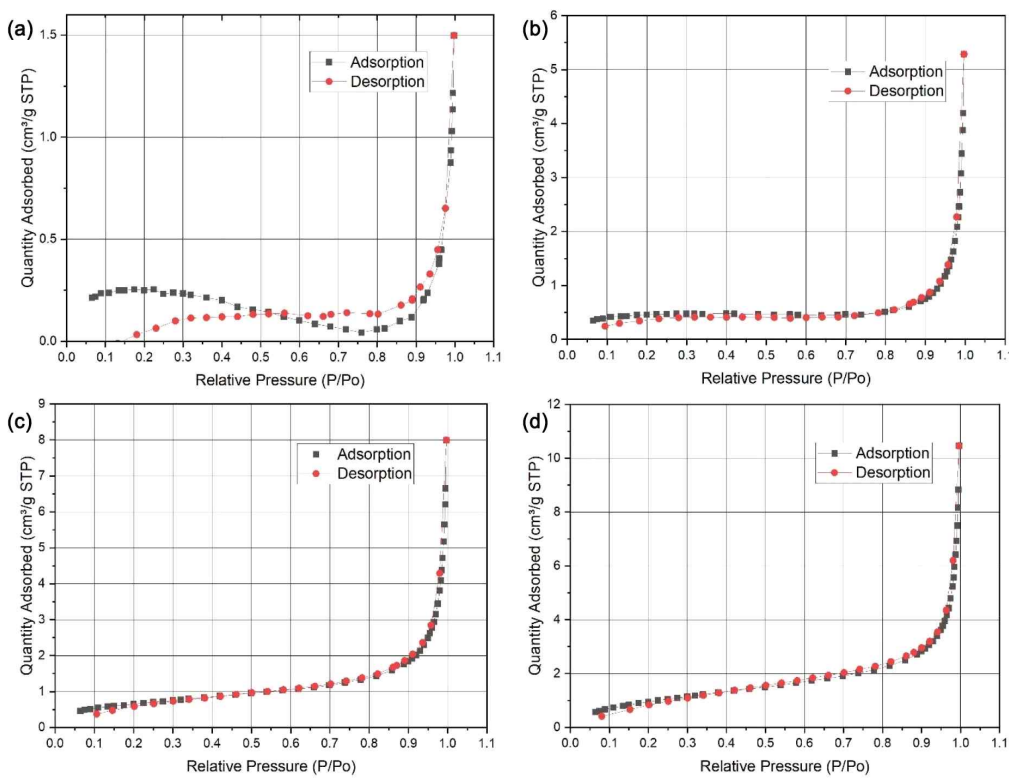

Fig. 6. BET analysis of (a) SCPFe0, (b) SCPFe10, (c) SCPFe20, and (d) SCPFe30. STP: standard temperature and pressure, BET: Brunauer Emmett Teller, SCP: sawdust cellulose powder.

genous surface. In all samples, the relative pressure (P/P0) is in the range from 0.1 to 1.0. The quantity of adsorbed nitrogen gas in SCP increases after adding Fe_3O_4-NPs which are 1.6618 cm^3/g STP, 4.2363 cm^3/g STP, 7.3649 cm^3/g STP, 10.3347 cm^3/g STP for SCPFe0, SCPFe10, SCPFe20, and SCPFe30, respectively. SCP with higher content of Fe_3O_4-NPs results in higher surface area with increasing BET surface area by about 310% from 0.9458 to 3.8853 m^2/g for SCPFe0 to SCPFe30 (Table 3).

The pore size and surface area of BET analysis are given in Table 3. The pore size of SCP is under 20 nm. The higher content of Fe_3O_4-NPs, lower pore size, and higher pore volume. The pore sizes of SCP composite are 9.608−16.6695 nm and pore volume ranging from 1,912−14,187 mm^3/g. This result is similar to the reported study that adding Fe_3O_4-NPs in the SCP can increase the surface area and porosity (Alizadeh and Rezaee, 2022; Tipsawat *et al.*, 2018).

3.6. Dye removal

The result of calculating dye removal (Rd) using Equation (3) is shown in Fig. 7. Rd indicates that SCPFe0 adsorb the Methylene Blue from polluted water till 96.1 ± 0.43% (0.388 ± 0.0017 mg/g), and SCPFe10, SCPFe20, and SCPFe30 adsorb Methylene Blue till 94.5 ± 0.62% (0.382 ± 0.0024 mg/g), 92.8 ± 0.38% (0.373 ± 0.0014 mg/g), and 89.7 ± 0.98% (0.359 ± 0.0035 mg/g) or the adsorption capacity is reduced as much as 1.7%, 3.4%, and 6.7% compared to SCPFe0, respectively. This Methylene Blue adsorption is smaller than carbon produced from Sapwood waste, that achieve. Otherwise, the Rd of PCFe0 for Congo Red dye is 53.1 ± 0.21% (0.224 ± 0.0005 mg/g). The other samples, such as SCPFe10, SCPFe20, and SCPFe30, Rd of Congo Red dye by 58.3 ± 0.10% (0.246 ± 0.0003 mg/g), 62.6 ± 0.43% (0.264 ± 0.0011 mg/g), and 70.0 ± 0.43% (0.295 ± 0.0013 mg/g). The adsorption capacity increased for Congo Red dye adsorption by 9.8%, 17.9%, and 31.8% compared to SCPFe0. One-way ANOVA analysis with a significant level of 95% indicates that the concentration of Fe_3O_4-NPs in SCP significantly impacts the adsorption of Methylene Blue (P_{value} = 0.00) and Congo Red dye (P_{value}

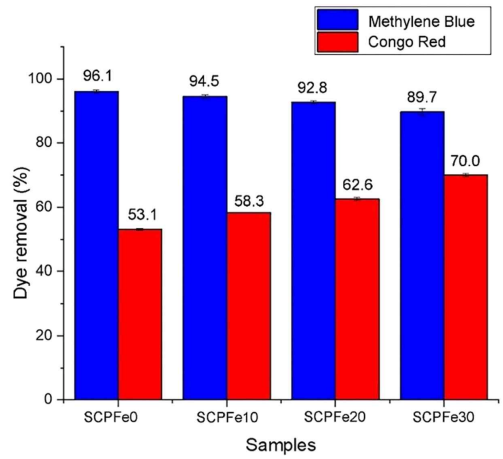

Fig. 7. Dye removal by magnetic SCP. SCP: sawdust cellulose powder.

Table 3. BET analysis outcomes concerning specific surface and area pore size

Sample	Pore volume (mm^3/g)	Pore diameter (nm)	BET surface area (m^2/g)
SCPFe0	1,912	16.6695	0.9458
SCPFe10	6,729	12.2163	1.5894
SCPFe20	10,619	11.8957	2.4160
SCPFe30	14,187	9.6080	3.8853

BET: Brunauer Emmett Teller, SCP: sawdust cellulose powder.

= 0.00).

The effect of magnetic nanoparticle content on the adsorption capacity is shown in Fig. 8. The kinetic evolution of the removal process of the dye by SCP composite was determined by experimental testing with time varying between 0 and 25 minutes, as depicted in Fig. 8. It was observed that the amount of dye adsorption increases with the contact time for all SCP composite samples. Until the contact time of 25 min, SCPFe30 and SCPFe10 have the highest amount of adsorption for Methylene Blue and Congo Red dye, respectively.

Fe_3O_4-NPs naturally possess hydroxyl groups on their surfaces because water dissociatively chemisorbs onto magnetite surfaces (Kendelewicz *et al.*, 2000). Increasing Fe_3O_4-NPs content, enhance Fe_3O_4-NP interactions so the number of hydroxyl groups in the SPC was increased (Fig. 4). This hydroxyl group facilitates an effective dye absorption by SPC to anionic dye like Congo Red, due to electrostatic and hydrogen bonding interaction and between the adsorbent and dyes. Additionally, electrostatic forces between the surface of Fe_3O_4-NPs and SPC contribute to another form of intermolecular bonding. These electrostatic interactions are advantageous for dye adsorption (Talbot *et al.*, 2021). Foroutan *et al.* (2021) reported that adding Fe_3O_4 in activated carbon causes increasing magnetic saturation and result in better adsorption capacity. Increasing the pore volume (Table 3) will generally increase the total capacity of adsorbent material to capture and store adsorbent substances. A larger pore volume provides a larger space to accommo-

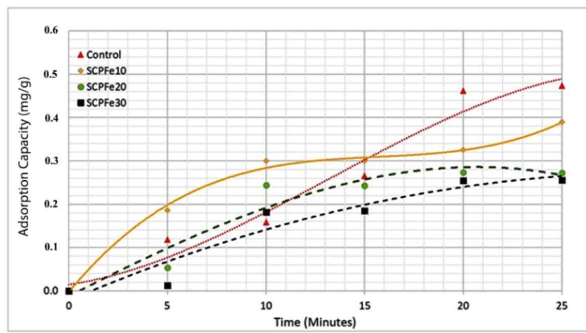

(a)

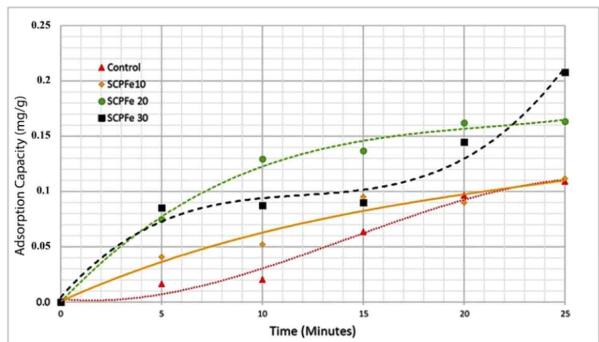

(b)

Fig. 8. Dye adsorption capacity of magnetic SCP. (a) Methylene Blue; (b) Congo Red. SCP: sawdust cellulose powder.

date adsorbent molecules, thereby increasing the adsorption capacity per unit mass of adsorbent. The larger the surface area of an adsorbent, the higher its adsorption capacity, as it can accommodate a larger quantity of adsorbate (Lawtae and Tangsathitkulchai, 2021).

The plotting results of the adsorption using pseudo-first order and pseudo-second order kinetic models at different magnetic content are shown in Fig. 9. In the form of straight-line equations for each kinetic model, the kinetic constants can be determined for each adsorption model used.

The results of kinetic data of the adsorption of Methylene Blue and Congo Red dye on SCP calculated using Equations (4) and (5) are tabulated in Table 4. The analysis of dye reaction kinetics at each concentration of Fe_3O_4-NPs shows that the adsorption process of Methylene Blue and Congo Red dyes in solution for each solution concentration has a different pattern. The Methylene Blue and Congo Red adsorption using the SPCFe adsorbent refers to a pseudo-first-order kinetic model instead of pseudo-second-order model because the correlation coefficient (R^2) obtained for the first order is between 0.6981−0.9094 and 0.7065−0.9402 for Methylene Blue and Congo Red dyes, respectively, while R^2 for second order has an extensive range between 0.0006−0.9478 and 0.3441−0.9772 for Methylene Blue and Congo Red dyes, respectively. The low value of R^2 in pseudo-second-order model indicate that this model is not fit with kinetic model in adsorption of SPC with functionalized by Fe_3O_4-NPs. The pseudo-first-order

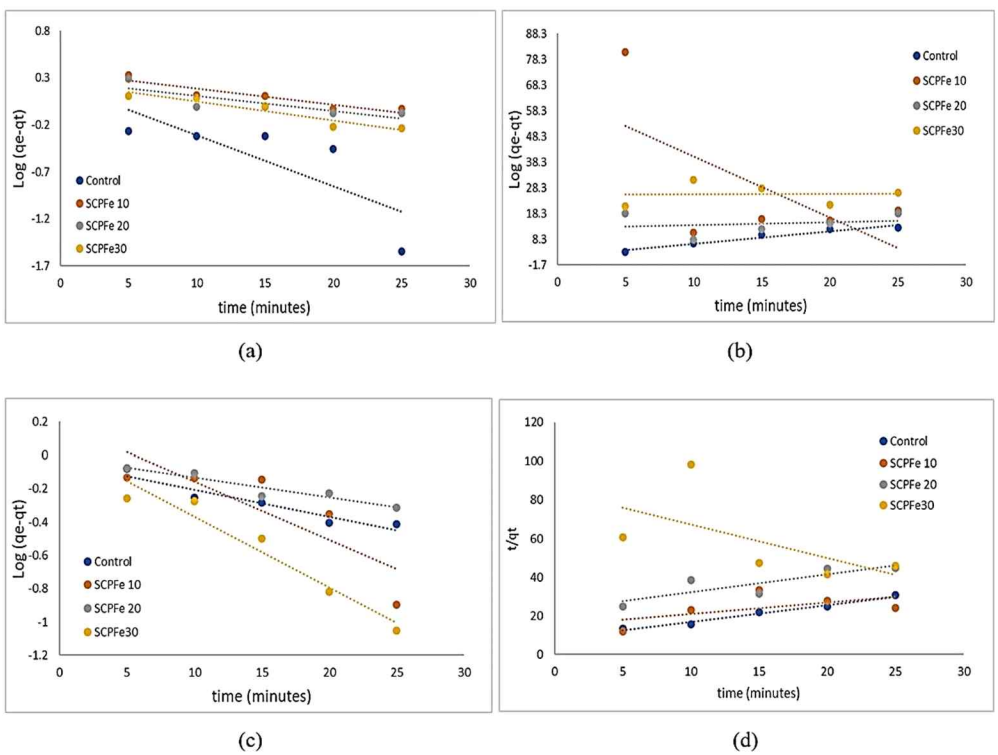

Fig. 9. Kinetic plots with linear regressions for SCP composite with different content of Fe_3O_4-NPs for the adsorption model of Methylene Blue. (a) Pseudo-first-order and (b) Pseudo-second-order; Congo Red: (c) Pseudo-first-order; (d) Pseudo-second-order. SCP: sawdust cellulose powder, Fe_3O_4-NPs: Fe_3O_4 nanoparticles.

kinetic model appears to be the better fit for both Methylene Blue and Congo Red adsorption. It suggests that the pseudo-first-order model is more robust and reliable in describing the adsorption kinetics with SPCFe adsorbent. This model indicate that adsorption occurs only physically without any chemical adsorption tendency (Khamizov, 2020). By increasing Fe_3O_4-NPs, the amount of adsorption increased for the anionic dye type (Congo Red) and decreased for the cationic dye type [Methylene Blue; Fig. 8(a) and (b)]. It indicates that only physical interaction resulted from the electrostatic force between the positive charge of Fe_3O_4-NPs surface and a negative charge from anionic dyes. It is supported by the calculation of a pseudo-first-order model of dye adsorption (Table 4).

Those materials (cellulose and its magnetic cellulose adsorbent) had different characteristics that could be used in the dye adsorption. The SCP has the ability to adsorb cationic dye types such as Methylene Blue easily because SCP contains hydroxyl groups that are scattered in the whole molecule (Oh and Park, 2022). The cationic dye-cellulose interaction occurs through hydrogen bonding and intermolecular Van der Waals forces (Akter *et al.*, 2021). Adding magnetic nanoparticles reduces cationic dye adsorption caused by reducing hydrophilic properties of SCP after interaction with magnetic nanoparticles. Different results were shown by anionic dyes like Congo Red. Anionic dyes have a repulsion to the

Table 4. Kinetic model constants and correlation coefficients for the adsorption of Methylene Blue and Congo Red dye on SCP

Dye	Samples	Pseudo first order			Pseudo second order			Ref.
		q_e (mg/g)	K1 (1/min)	R^2	q_e (mg/g)	K2 (g/mg/min)	R^2	
Methylene Blue	Control	1.9763	0.1244	0.9054	2.0567	2.386	0.9478	This study
	SCPFe 10	0.1926	0.0806	0.7065	0.4218	0.0027	0.4045	
	SCPFe 20	2.2085	0.0366	0.6981	8.3263	5.5031	0.0483	
	SCPFe 30	1.5308	0.0458	0.9094	71.4285	199.579	0.0006	
Congo Red	Control	1.2044	0.0375	0.9054	1.1470	0.1621	0.9772	This study
	SCPFe 10	1.1664	0.0806	0.7065	1.7027	0.3572	0.3431	
	SCPFe 20	1.0459	0.0274	0.8947	1.0800	0.1437	0.7130	
	SCPFe 30	0.6339	0.0981	0.9402	0.5766	0.0410	0.3441	
Crystal Violet	Biochar	14.9	0.044	0.817	16.4	0.00321	0.884	Kyi *et al.* (2020)
Methylene Blue	Rice husk	17.1038	0.028	0.9848	18.1906	0.0026	0.9641	Quansah *et al.* (2020)
Methylene Blue	Annona squmosa seed	3.5859	0.037	0.927	4.2937	0.00113	0.9889	Santhi *et al.* (2016)
Acid Yellow 29	Ailanthus altissima sawdust	9.467	-5×10^{-6}	0.9974	0.00179	121,876	0.9999	Rahman *et al.* (2021)

SCP: sawdust cellulose powder.

hydroxyl group in SCP, but after the addition of magnetic nanoparticles, Congo Red adsorption increases up to 31.8% (Yu *et al.*, 2014). It is caused by magnetic nanoparticles having a positive charge at a neutral aqueous solution, so they easily interact with Conge Red dye as anionic dye, so Congo Red adsorption increases after adding Fe_3O_4-NPs into SCP.

4. CONCLUSIONS

The effect of Fe_3O_4-NPs on sawdust waste was examined. The SCP's surface structure revealed that Fe_3O_4-NPs were deposited and distributed throughout. A larger concentration of Fe_3O_4-NPs resulted in agglomerates on the surface. The analysis of functional groups at specified wavenumbers (1,156 cm^{-1} to 1,589 cm^{-1}) revealed an interaction between SCP and Fe_3O_4-NPs. The addition of Fe_3O_4-NPs caused a modest drop in the nanocomposite's CI. Interestingly, SCP's crystal size rose from 12.18 to 15.75 nm. BET research revealed that the SCP composite had a mesoporous surface, with pore sizes ranging from 9.6080 to 16.6695 nm. The introduction of Fe_3O_4-NPs into the SCP resulted in significant modifications to its magnetic characteristics. Specifically, the SCP, which was previously diamagnetic, changed to a magnetic state with superparamagnetic properties, as demonstrated by a modest hysteresis curve in VSM analysis. Adding magnetic nanoparticles boosted their ability to adsorb anionic dyes such as Congo Red by up to 31.8%, and the adsorption of SCP composite for Methylene Blue and Congo Red dye tends to follow a pseudo-first-order adsorption kinetics model. In the future, SCP enhanced with magnetic nanoparticles may be used as a dye adsorbent for wastewater treatment.

CONFLICT of INTEREST

No potential conflict of interest relevant to this article was reported.

ACKNOWLEDGMENT

The authors sincerely express their heartfelt thanks to Universitas Negeri Malang for the research grant funded by non-APBN budget by contract no. 5.4.814/UN32.20.1/LT/2023.

REFERENCES

Akter, M., Bhattacharjee, M., Dhar, A.K., Rahman, F.B.A., Haque, S., Ur Rashid, T.U., Kabir, S.M.F. 2021. Cellulose-based hydrogels for wastewater treatment: A concise review. Gels 7(1): 1-28.

Al-Harby, N.F., Albahly, E.F., Mohamed, N.A. 2021. Kinetics, isotherm and thermodynamic studies for efficient adsorption of congo red dye from aqueous solution onto novel cyanoguanidine-modified chitosan adsorbent. Polymers 13(24): 4446.

Alizadeh, Z., Rezaee, A. 2022. Tetracycline removal using microbial cellulose@nano-Fe_3O_4 by adsorption and heterogeneous Fenton-like processes. Journal of Molecular Liquids 366: 120199.

Barros, A., Vecino, X., Reig, M., Cortina, J.L. 2022. Coagulation and flocculation optimization process applied to the sidestream of an urban wastewater treatment plant. Water 14(24): 4024.

Bhuiyan, M.T.R., Hirai, N., Sobue, N. 2000. Changes of crystallinity in wood cellulose by heat treatment under dried and moist conditions. Journal of Wood Science 46(6): 431-436.

Daoush, W.M. 2017. Co-precipitation and magnetic properties of magnetite nanoparticles for potential biomedical applications. Journal of Nanomedicine Research 5(3): 00118.

Dong, Y., Yan, Y., Zhang, Y., Zhang, S., Li, J. 2016. Combined treatment for conversion of fast-growing poplar wood to magnetic wood with high dimensional stability. Wood Science and Technology 50(3): 503-517.

Elsacker, E., Vandelook, S., Damsin, B., Van Wylick, A., Peeters, E., De Laet, L. 2021. Mechanical characteristics of bacterial cellulose-reinforced mycelium composite materials. Fungal Biology and Biotechnology 8(1): 1-14.

Foroutan, R., Peighambardoust, S.J., Peighambardoust, S.H., Pateiro, M., Lorenzo, J.M. 2021. Adsorption of crystal violet dye using activated carbon of lemon wood and activated carbon/Fe_3O_4 magnetic nanocomposite from aqueous solutions: A kinetic, equilibrium and thermodynamic study. Molecules 26(8): 2241.

Fortune Business Insight. 2024. Cellulose market size, share and industry analysis and regional forecast 2019-2026. https://www.fortunebusinessinsights.com/cellulose-market-102062

Giacobbo, A., Bernardes, A.M. 2022. Membrane separation process in wastewater and water purification. Membranes 12(3): 259.

Groeneveld, I., Kanelli, M., Ariese, F., van Bommel, M.R. 2023. Parameters that affect the photodegradation of dyes and pigments in solution and on substrate: An overview. Dyes and Pigments 210: 110999.

Gwon, J.G., Lee, D.B., Cho, H.J., Lee, S.Y. 2018. Preparation and characteristics of cellulose acetate based nanocomposites reinforced with cellulose nanocrystals (CNCs). Journal of the Korean Wood Science and Technology 46(5): 565-576.

Hadi, Y.S., Massijaya, M.Y., Abdillah, I.B., Pari, G., Arsyad, W.O.M. 2020. Color change and resistance to subterranean termite attack of mangium (*Acacia mangium*) and sengon (*Falcataria moluccana*) smoked wood. Journal of the Korean Wood Science and Technology 48(1): 1-11.

Hanafi, M.F., Sapawe, N. 2020. A review on the water problem associate with organic pollutants derived from phenol, methyl orange, and remazol brilliant blue dyes. Materials Today: Proceedings 31(Part 1): A141-A150.

Haryanto, A., Hidayat, W., Hasanudin, U., Iryani, D.A., Kim, S., Lee, S., Yoo, J. 2021. Valorization of Indonesian wood wastes through pyrolysis: A review. Energies 14(5): 1-25.

Hussain, A., Li, J., Wang, J., Xue, F., Chen, Y., Bin Aftab, T., Li, D. 2018. Hybrid monolith of graphene/TEMPO-oxidized cellulose nanofiber as mechanically robust, highly functional, and recyclable adsorbent of methylene blue dye. Journal of Nanomaterials 2018: 5963982.

Hwang, J.W., Oh, S.W. 2020. Mechanical performances of boards made from carbonized rice husk and sawdust: The effect of resin and sawdust addition ratio. Journal of the Korean Wood Science and Technology 48(5): 696-709.

Hwang, J.W., Oh, S.W. 2021. Bending strength of board manufactured from sawdust, rice husk and charcoal. Journal of the Korean Wood Science and Technology 49(4): 315-327.

Hwang, J.W., Oh, S.W. 2023. Mechanical properties and density profile of ceramics manufactured from a board mixed with sawdust and mandarin peels. Journal of the Korean Wood Science and Technology 51(2): 98-108.

Hwang, J.W., Oh, S.W. 2024. Density profile and sound absorption capability of ceramics manufactured from sawdust, chaff and charcoal: Effect of carbonization temperature and mixing ratio. Journal of the Korean Wood Science and Technology 52(3): 234-242.

Ivanova, O.S., Edelman, I.S., Lin, C.R., Svetlitsky, E.S., Sokolov, A.E., Lukyanenko, K.A., Sukhachev, A.L., Shestakov, N.P., Chen, Y.Z., Spivakov, A.A. 2023. Core–shell Fe_3O_4@C nanoparticles for the organic dye adsorption and targeted magneto-mechanical destruction of ehrlich ascites carcinoma cells. Materials 16(1): 23.

Jiang, C., Cui, S., Han, Q., Li, P., Zhang, Q., Song, J., Li, M. 2019. Study on application of activated

carbon in water treatment. IOP Conference Series: Earth and Environmental Science 237(2): 022049.

Kamakshi, T., Sundari, G.S., Erothu, H., Singh, R.S. 2019. Effect of nickel dopant on structural, morphological and optical characteristics of Fe_3O_4 nanoparticles. Rasāyan Journal of Chemistry 12(2): 531-536.

Kameya, Y., Yabe, H. 2019. Optical and superhydrophilic characteristics of TiO_2 coating with subwavelength surface structure consisting of spherical nanoparticle aggregates. Coatings 9(9): 547.

Kędzierska, M., Potemski, P., Drabczyk, A., Kudłacik-Kramarczyk, S., Głąb, M., Grabowska, B., Mierzwiński, D., Tyliszczak, B. 2021. The synthesis methodology of PEGylated Fe_3O_4@Ag nanoparticles supported by their physicochemical evaluation. Molecules 26(6): 1744.

Kemp, S. 2023. Digital 2023: Indonesia. https://datareportal.com/reports/digital-2023-indonesia

Kendelewicz, T., Liu, P., Doyle, C.S., Brown, G.E. Jr., Nelson, E.J., Chambers, S.A. 2000. Reaction of water with the (100) and (111) surfaces of Fe_3O_4. Surface Science 453(1-3): 32-46.

Khamizov, R.K. 2020. A pseudo-second order kinetic equation for sorption processes. Russian Journal of Physical Chemistry A 94(1): 171-176.

Kheradmand, A., Negarestani, M., Mollahosseini, A., Shayesteh, H., Farimaniraad, H. 2022. Low-cost treated lignocellulosic biomass waste supported with $FeCl_3$/$Zn(NO_3)_2$ for water decolorization. Scientific Reports 12(1): 16442.

Kiangkitiwan, N., Srikulkit, K. 2021. Preparation and properties of bacterial cellulose/graphene oxide composite films using dyeing method. Polymer Engineering & Science 61(6): 1854-1863.

Koshani, R., Tavakolian, M., van de Ven, T.G.M. 2020. Cellulose-based dispersants and flocculants. Journal of Materials Chemistry B 8(46): 10502-10526.

Kyi, P.P., Quansah, J.O., Lee, C.G., Moon, J.K., Park, S.J. 2020. The removal of crystal violet from textile wastewater using palm kernel shell-derived biochar. Applied Sciences 10(7): 2251.

Laksono, G.D., Rahayu, I.S., Karlinasari, L., Darmawan, W., Prihatini, E. 2023. Characteristics of magnetic sengon wood impregnated with nano Fe_3O_4 and furfuryl alcohol. Journal of the Korean Wood Science and Technology 51(1): 1-13.

Lawtae, P., Tangsathitkulchai, C. 2021. The use of high surface area mesoporous-activated carbon from longan seed biomass for increasing capacity and kinetics of methylene blue adsorption from aqueous solution. Molecules 26(21): 6521.

Lee, C.M., Gu, J., Kafle, K., Catchmark, J., Kim, S.H. 2015. Cellulose produced by *Gluconacetobacter xylinus* strains ATCC 53524 and ATCC 23768: Pellicle formation, post-synthesis aggregation and fiber density. Carbohydrate Polymers 133: 270-276.

Lee, K.E., Morad, N., Teng, T.T., Poh, B.T. 2012. Development, characterization and the application of hybrid materials in coagulation/flocculation of wastewater: A review. Chemical Engineering Journal 203: 370-386.

Lesiak, B., Rangam, N., Jiricek, P., Gordeev, I., Tóth, J., Kövér, L., Mohai, M., Borowicz, P. 2019. Surface study of Fe_3O_4 nanoparticles functionalized with biocompatible adsorbed molecules. Frontiers in Chemistry 7: 642.

Li, Z., Gong, W., Chen, X., Liu, L., Meng, R., Ding, Y., Yao, J. 2021. Sustainable cationic cellulose for highly efficient flocculation of Kaolin suspension. Cellulose 28(17): 11097-11108.

Mahsuli, T., Larasati, A., Aminnudin, A., Maulana, J. 2023. Effect of the homogenization process on titanium oxide-reinforced nanocellulose composite membranes. Journal of Mechanical Engineering Science and Technology 7(2): 137-146.

Mindaryani, A., Sulton, A., Setiawan, F.A., Rahayuningsih, E. 2023. Natural dye extraction from Merbau (*Intsia*

bijuga) sawdust: Optimization of solid–solvent ratio and temperature. Journal of the Korean Wood Science and Technology 51(6): 481-492.

Mitić, Ž., Nikolić, G.S., Cakić, M., Premović, P., Ilić, L. 2009. FTIR spectroscopic characterization of Cu(II) coordination compounds with exopolysaccharide pullulan and its derivatives. Journal of Molecular Structure 924–926: 264-273.

Movagharnezhad, N., Ehsanimehr, S., Moghadam, P.N. 2022. Synthesis of poly (N-vinylpyrrolidone)-grafted-magnetite bromoacetylated cellulose via ATRP for drug delivery. Material Chemistry Horizons 1(2): 89-98.

Mwango, A., Kambole, C. 2019. Engineering characteristics and potential increased utilisation of sawdust composites in construction: A review. Journal of Building Construction and Planning Research 7(3): 59-88.

Nindiyasari, F., Griesshaber, E., Zimmermann, T., Manian, A.P., Randow, C., Zehbe, R., Fernandez-Diaz, L., Ziegler, A., Fleck, C., Schmahl, W.W. 2016. Characterization and mechanical properties investigation of the cellulose/gypsum composite. Journal of Composite Materials 50(5): 657-672.

Nithya, R., Thirunavukkarasu, A., Sathya, A.B., Sivashankar, R. 2021. Magnetic materials and magnetic separation of dyes from aqueous solutions: A review. Environmental Chemistry Letters 19(2): 1275-1294.

Oh, J.E., Park, N.M. 2022. Hydrophilic, transparent, and stretchable film using unmodified cellulose fibers. Materials Letters 309: 131385.

Padmanabhan, N.T., Thomas, N., Louis, J., Mathew, D.T., Ganguly, P., John, H., Pillai, S.C. 2021. Graphene coupled TiO_2 photocatalysts for environmental applications: A review. Chemosphere 271: 129506.

Palanisamy, S., Wang, Y.M. 2019. Superparamagnetic iron oxide nanoparticulate system: Synthesis, targeting, drug delivery and therapy in cancer. Dalton Transactions 48(26): 9490-9515.

Quansah, J.O., Hlaing, T., Lyonga, F.N., Kyi, P.P., Hong, S.H., Lee, C.G., Park, S.J. 2020. Nascent rice husk as an adsorbent for removing cationic dyes from textile wastewater. Applied Sciences 10(10): 3437.

Rahman, N.U., Ullah, I., Alam, S., Khan, M.S., Shah, L.A., Zekker, I., Burlakovs, J., Kallistova, A., Pimenov, N., Vincevica-Gaile, Z., Jani, Y., Zahoor, M. 2021. Activated *Ailanthus altissima* sawdust as adsorbent for removal of acid yellow 29 from wastewater: Kinetics approach. Water 13(15): 2136.

Rahman, N.U., Bahadar, W., Alam, S., Zahoor, M., Zekker, I., Khan, F.A., Ullah, R., Ali, E.A., Murthy, H.C.A. 2022. Activated sawdust-based adsorbent for the removal of basic blue 3 and methylene green from aqueous media. Adsorption Science & Technology 2022: 4551212.

Rahmawati, R., Taufiq, A., Sunaryono, S., Fuad, A., Yuliarto, B., Suyatman, S., Kurniadi, D. 2018. Synthesis of magnetite (Fe_3O_4) nanoparticles from iron sands by coprecipitation-ultrasonic irradiation methods. Journal of Materials and Environmental Science 9(1): 155-160.

Rani, M., Shanker, U. 2023. Removal of Organic Dyes by Functionalized Nanomaterials. In: Handbook of Green and Sustainable Nanotechnology: Fundamentals, Developments and Applications, Ed. by Shanker, U., Hussain, C.M., and Rani, M. Springer, Cham, Switzerland.

Rashid, R., Shafiq, I., Akhter, P., Iqbal, M.J., Hussain, M. 2021. A state-of-the-art review on wastewater treatment techniques: The effectiveness of adsorption method. Environmental Science and Pollution Research 28(8): 9050-9066.

Renu, Agarwal, M., Singh, K. 2017. Heavy metal removal from wastewater using various adsorbents: A review. Journal of Water Reuse and Desalination 7(4): 387-419.

Santhi, T., Manonmani, S., Vasantha, V.S., Chang, Y.T. 2016. A new alternative adsorbent for the removal of cationic dyes from aqueous solution. Arabian Journal of Chemistry 9(Supplement 1): S466-S474.

Sezer, N., Arı, İ., Biçer, Y., Koç, M. 2021. Superparamagnetic nanoarchitectures: Multimodal functionalities and applications. Journal of Magnetism and Magnetic Materials 538: 168300.

Sharma, S.K. 2015. Green Chemistry for Dyes Removal from Waste Water: Research Trends and Applications. John Wiley & Sons, Hoboken, NJ, USA.

Stefan, D.S., Bosomoiu, M., Stefan, M. 2022. Methods for natural and synthetic polymers recovery from textile waste. Polymers 14(19): 3939.

Suciyati, S.W., Manurung, P., Sembiring, S., Situmeang, R. 2021. Comparative study of *Cladophora* sp. cellulose by using FTIR and XRD. Journal of Physics: Conference Series 1751(1): 012075.

Sukmana, H., Bellahsen, N., Pantoja, F., Hodur, C. 2021. Adsorption and coagulation in wastewater treatment: Review. Progress in Agricultural Engineering Sciences 17(1): 49-68.

Suryanto, H., Kurniawan, F., Syukri, D., Binoj, J.S., Hari, P.D., Yanuhar, U. 2023. Properties of bacterial cellulose acetate nanocomposite with TiO_2 nanoparticle and graphene reinforcement. International Journal of Biological Macromolecules 235: 123705.

Suryanto, H., Sukarni, S., Rohmat, Y., Pradana, A., Yanuhar, U., Witono, K. 2019. Effect of mercerization on properties of mendong (*Fimbristylis globulosa*) fiber. Songklanakarin Journal of Science and Technology 41(3): 624-630.

Sutapa, J.P.G., Lukmandaru, G., Sunarta, S., Pujiarti, R., Irawati, D., Arisandi, R., Dwiyanna, R., Priyambodo, R.D. 2024. Utilization of sapwood waste of fast-growing teak in activated carbon production and its adsorption properties. Journal of the Korean Wood Science and Technology 52(2): 118-133.

Talbot, D., Queiros Campos, J., Checa-Fernandez, B.L., Marins, J.A., Lomenech, C., Hurel, C., Godeau, G.D., Raboisson-Michel, M., Verger-Dubois, G., Obeid, L., Kuzhir, P., Bee, A. 2021. Adsorption of organic dyes on magnetic iron oxide nanoparticles. Part I: Mechanisms and adsorption-induced nanoparticle agglomeration. ACS Omega 6(29): 19086-19098.

Teixeira, R.A., Lima, E.C., Benetti, A.D., Thue, P.S., Cunha, M.R., Cimirro, N.F.G.M., Sher, F., Dehghani, M.H., dos Reis, G.S., Dotto, G.L. 2021. Preparation of hybrids of wood sawdust with 3-aminopropyltriethoxysilane. Application as an adsorbent to remove reactive blue 4 dye from wastewater effluents. Journal of the Taiwan Institute of Chemical Engineers 125: 141-152.

Thangavelu, K., Zou, L. 2022. Evaluating oil removal by amphiphilic MoS_2/cellulose acetate fibrous sponge in a flow-through reactor and by artificial neural network. Environmental Nanotechnology, Monitoring & Management 18: 100684.

Tipsawat, P., Wongpratat, U., Phumying, S., Chanlek, N., Chokprasombat, K., Maensiri, S. 2018. Magnetite (Fe_3O_4) nanoparticles: Synthesis, characterization and electrochemical properties. Applied Surface Science 446: 287-292.

Upadhyay, S., Parekh, K., Pandey, B. 2016. Influence of crystallite size on the magnetic properties of Fe_3O_4 nanoparticles. Journal of Alloys and Compounds 678: 478-485.

Usawattanakul, N., Torgbo, S., Sukyai, P., Khantayanuwong, S., Puangsin, B., Srichola, P. 2021. Development of nanocomposite film comprising of polyvinyl alcohol (PVA) incorporated with bacterial cellulose. Polymers 13(11): 1778.

Widyarani, Wulan, D.R., Hamidah, U., Komarulzaman, A., Rosmalina, R.T., Sintawardani, N. 2022. Domestic wastewater in Indonesia: Generation, characteristics and treatment. Environmental Science and Pollution Research 29(22): 32397-32414.

Wiguna, C.S., Suryanto, H., Aminuddin, Maulana, J., Binoj, J.S., Ali, A. 2023. Effect of grafting nano-TiO_2 on *Sansevieria cylindrica* fiber properties. Journal of Mechanical Engineering Science and Technology 7(1): 10-19.

Wotton, A., Yeung, T., Jennepalli, S., Teh, Z.L., Pickford, R., Huang, S., Conibeer, G., Stride, J.A., Patterson, R.J. 2021. Simultaneous Fe_3O_4 nanoparticle formation and catalyst-driven hydrothermal cellulose degradation. ACS Omega 6(16): 10790-10800.

Xiao, Y., Du, J. 2020. Superparamagnetic nanoparticles for biomedical applications. Journal of Materials Chemistry B 8(3): 354-367.

Yamklang, W., Prada, T., Bunriw, W., Kaeochana, W., Harnchana, V. 2023. Fe_3O_4-filled cellulose paper for triboelectric nanogenerator application. Polymers 15(1): 94.

Yang, I., Jeong, H., Lee, J.J., Lee, S.M. 2019. Relationship between lignin content and the durability of wood pellets fabricated using *Larix kaempferi* C. sawdust. Journal of the Korean Wood Science and Technology 47(1): 110-123.

Yanuhar, U., Suryanto, H., Sardjono, S.A., Ningrum, I.K., Aminnudin, A., Binoj, J.S. 2022. Effect of titanium dioxide nanoparticle on properties of nanocomposite membrane made of bacterial cellulose. Journal of Natural Fibers 19(16): 13914-13927.

Yu, H., Li, Y., Li, X., Fan, L., Yang, S. 2014. Highly dispersible and charge-tunable magnetic Fe_3O_4 nanoparticles: Facile fabrication and reversible binding to GO for efficient removal of dye pollutants. Journal of Materials Chemistry A 2(38): 15763-15767.

Yu, S., Sun, J., Shi, Y., Wang, Q., Wu, J., Liu, J. 2021. Nanocellulose from various biomass wastes: Its preparation and potential usages towards the high value-added products. Environmental Science and Ecotechnology 5: 100077.

Zhang, Y., Li, J., Ma, N., Meng, Z., Sui, G. 2019. Processing cellulose@Fe_3O_4 into mechanical, magnetic and biodegradable synapse-like material. Composites Part B: Engineering 177: 107432.